https://doi.org/10.1016/j.compstruct.2021.114329

Compound Concrete-Filled FRP Tubular Columns under Cyclic Axial Compression

J.K. Zhou[1], Guan Lin[2,*], J.G. Teng[3], F.ASCE

Abstract: The direct use of large pieces of crushed demolition concrete (referred to as recycled concrete lumps or RCLs) for mixing with fresh concrete to create a new kind of recycled concrete (referred to as compound concrete), has obvious advantages in terms of recycling efficiency, cost-effectiveness and maximum recycling ratio compared with the recycling of concrete as aggregates. Existing research has revealed certain performance concerns with such compound concrete, including reductions in strength and durability, due to the presence of RCLs. The confinement of compound concrete with an external fiber-reinforced polymer (FRP) confining tube has recently been explored as an effective technique to improve its mechanical properties and durability. This paper presents the results of the first ever experimental study on compound concrete filled FRP tubular (CCFFT) columns aimed at the understanding and modelling of the cyclic stress-strain behavior of FRP-confined compound concrete. The effects of RCL mix ratio, FRP tube thickness, and loading scheme are examined. A monotonic stress-strain model and two cyclic stress-strain models previously developed for FRP-confined normal concrete are used to predict the test results. It is shown that the inclusion of RCLs has a marginal effect on the cyclic stress-strain behavior of FRP-confined concrete.

Keywords: Fiber reinforced polymer (FRP); Recycled concrete lump (RCL); Stress-strain behavior; Filament-wound FRP tube; Confinement; Cyclic loading.

1. Introduction

A typical method of using demolition concrete is to recycle it into concrete aggregates, which are then used in making new concrete (referred to as recycled aggregate concrete or RAC). In a typical RAC, the natural coarse aggregate is partially or completely replaced with recycled coarse aggregate (RCA). A significant number of studies have been conducted on the use of RAC in structural members (e.g. [1-8]). The existing research has concluded that the presence of RCA leads to inferior performance of the concrete, including reductions in strength and stiffness as well as increases in creep and shrinkage, when compared with its natural aggregate concrete counterpart [2,9]. In addition, the recycling process of RCA involves crushing, screening and cleaning of aggregate, leading to a costly process, which limits the application of RAC.

More recently, Wu et al. [10] proposed a new recycling technique in which demolition concrete is coarsely broken into large lumps with a size of 50 mm to 300 mm (referred to as recycled concrete lumps or RCLs hereafter), which are then directly mixed with fresh concrete to create

[1] Postdoctoral Fellow, School of Civil and Transportation Engineering, Guangdong University of Technology, Guangzhou 510006, China; formerly, PhD Student, Department of Civil and Environmental Engineering, The Hong Kong Polytechnic University, Hong Kong, China. zhoujiekai@gdut.edu.cn
[2] Research Assistant Professor, Department of Civil and Environmental Engineering, The Hong Kong Polytechnic University, Hong Kong, China. (Corresponding author) guanlin@polyu.edu.hk
[3] Chair Professor of Structural Engineering, Department of Civil and Environmental Engineering, The Hong Kong Polytechnic University, Hong Kong, China. cejgteng@polyu.edu.hk

a new kind of recycled concrete; such recycled concrete has been referred to as compound concrete by Teng et al. [11]. This novel recycling technique has the following advantages over the traditional recycling method of converting demolition concrete into concrete aggregates [11,12]: (1) the recycling process is substantially simplified as the concrete is crushed only into large lumps; (2) the recycling ratio (ratio between the weight of the recycled portion and the total weight of the old concrete) can be significantly increased. The feasibility of the new recycling method has been demonstrated by Wu's research group through a series of experimental studies on structural members made of such compound concrete (e.g. [13-15]). However, it has been found that the presence of RCLs leads to reductions in the performance of concrete, especially when the strength of RCLs is lower than that of the fresh concrete, which is expected to be common in the practical application of this recycling technique. These negative effects of RCLs are mainly attributable to the weak interfaces between fresh concrete and RCLs, and the much greater heterogeneity of compound concrete compared to conventional concrete.

To reduce or eliminate the drawbacks associated with the use of RCLs, a promising method is to use compound concrete as the filler material in tubular columns, where the tube confines the compound concrete and isolates it from direct exposure to the ambient environment. Wu's research group has explored the use of compound concrete in concrete-filled steel tubular (CFST) columns through a series of experimental studies on such columns under different loading conditions (e.g., concentric/eccentric loading and cyclic lateral loading) [16-19] However, they have found that the detrimental effects of RCLs could not be fully eliminated partly because of the limited confinement provided by a steel tube [16,17]. More recently, Teng et al. [11,20] proposed the combination of fiber-reinforced polymer (FRP) tubes with compound concrete to form the so-called compound concrete-filled FRP tubular (CCFFT) columns. The fibers in such FRP tubes are oriented close to the hoop direction of the tube, so the tubes are strong and stiff in the hoop direction to provide confinement and shear resistance to CCFFT columns. The use of FRP tubes rather than steel tubes has the following advantages: (1) better confinement as the FRP tube has negligible axial resistance/stiffness so its lateral dilation is much smaller than the concrete core right from the beginning of loading; (2) better durability as the FRP tube has excellent corrosion resistance. To demonstrate the feasibility of the new approach, Teng et al. [11] and subsequently Zhou et al. [21] have presented systematic experimental investigations into CCFFT columns with different RCL mix ratios (i.e., the weight ratio of the RCLs and the compound concrete containing the RCLs) under monotonic axial compression. Their study revealed an additional but very important benefit offered by the FRP tube: due to FRP confinement, the ultimate axial stress and ultimate axial strain of the compound concrete become comparable to those of the fresh concrete even though the latter has a much higher strength than the RCLs. This observation means that FRP confinement can effectively eliminate the drawbacks associated with the use of RCLs. More importantly, this observation implies that although old concrete generally has a comparatively low compressive strength, the strength of the compound concrete is not limited or significantly affected by this low strength; instead, by using high strength fresh concrete with RCLs, the resulting compound concrete can be expected to be almost as strong as the fresh concrete under an appropriate level of confinement.

Only two studies [11,21] have been conducted on CCFFTs and both were concerned with monotonic axial compression. No study has been carried out on CCFFTs under cyclic axial compression. Such studies are essential for the understanding and modelling of the cyclic stress-strain behavior of FRP-confined compound concrete. Indeed, the cyclic stress-strain behavior of FRP-confined normal concrete has by now been extensively investigated and well understood (e.g. [22-28]). Against this background, the present paper presents the results of the first ever series of cyclic axial compression tests on CCFFT columns. The variables examined in the present study include the RCL mix ratio, the FRP tube thickness (i.e., the level of confinement), and the loading scheme. The cyclic axial stress-axial strain curves of FRP-confined compound concrete in the test CCFFT columns are also compared with predictions from two existing cyclic stress-strain models previously developed for FRP-confined normal concrete.

2. Experimental Program

2.1. Specimen Details

A total of 14 column specimens were prepared and tested, 12 of which were specimens confined with a glass FRP (GFRP) tube. Filament wound GFRP tubes were used as they are commercially available and can be used directly as molds for casting concrete. All the column specimens had a diameter of 200 mm and a height of 400 mm for the concrete core, and were confined with a 0-ply, 6-ply, or 9-ply GFRP tube. Three RCL mix ratios (i.e., 0%, 15%, and 30%). Three different loading schemes, including the monotonic axial compression scheme and two cyclic axial compression schemes, were employed. Table 1 provides the details of the specimens. Each specimen in Table 1 is given a name in the form of C*x*-R*y*-T*z*-M/C1/C2, where *x* represents the nominal compressive strength of fresh concrete, *y* represents the RCL mix ratio, and *z* represents the number of plies of the GFRP tube. The name ends with a letter M or C1/C2 to represent the monotonic loading scheme or one of the cyclic loading scheme.

2.2. Material Properties

2.2.1. RCLs and fresh concrete

The RCLs in the present experimental study were produced by crushing standard concrete cylinders (150 mm × 300 mm) into concrete lumps with the lump characteristic dimensions being between 60 mm and 100 mm (i.e., with RCLs retained on a test sieve of 60 mm mesh size and passing a test sieve of 100 mm mesh size). The concrete cylinders had been cured at room temperature for at least 28 days after casting before the crushing operation. The number of RCLs with a characteristic dimension of 80-100 mm was around twice the number of RCLs with a characteristic dimension of 60-80 mm. The compressive strength of the RCLs was found to be 41.8 MPa based on the compression tests of three concrete cylinders made of the same concrete as was used to produce the RCLs. The water absorptions in mass and density of the RCLs in the saturated surface-dry condition were measured to be 4.53% and 2.36 g/cm^3, respectively, in accordance with BS 812 [29] (Table 1). Figure 1 shows the photo of three RCLs with the typical highly irregular surfaces, where the mortar and the coarse aggregate particles of the old concrete can be clearly seen.

Three standard concrete cylinders were prepared and then tested at the same time of testing the column specimens to obtain the fresh concrete properties. The average compressive strength of fresh concrete was measured to be 90.9 MPa, which is much larger than the compressive strength of RCLs (41.8 MPa). The elastic modulus and the axial strain at peak stress of fresh concrete were 31363 MPa and 0.00329, respectively.

2.2.2. FRP tubes

Filament wound GFRP tubes made of E-glass fibers and unsaturated polyester resin from a supplier from Guangzhou, China, were used in the experimental program. The fibers were oriented at ± 81° to the longitudinal axis of the tube as specified by the manufacturer. The nominal thickness of fibers per ply of the tubes was 0.22 mm, while the actual thicknesses of the 6-ply and 9-ply GFRP tubes were 2.2 mm and 4.5 mm, respectively. The tensile properties of GFRP tubes in the hoop direction were obtained from tensile tests on curved coupons cut from a 6-ply GFRP tube segment with a width of 35 mm (Figure 2). The arc length of each curved coupon was 250 mm (corresponding to around 40% of the perimeter of the 200-mm-diameter tube). Three strain gauges (gauge length = 20 mm) were installed on each coupon, two on the inner surface at the mid-length (at 5 mm from the adjacent edge of the coupon) and one at the center of the outer surface (Figure 2b). Each end of the coupon was anchored into a laboratory-made clamping fixture with a clamping length of 50 mm (Figure 2b). The clamping fixtures were connected to an MTS machine through hinges which allowed the curved coupon ends to rotate freely during the loading process.

Figure 3a shows the typical experimental tensile stress-stain curves of a curved coupon, where the tensile stresses were obtained from the tensile forces divided by the cross-sectional area of the coupon based on its actual thickness, while the tensile strains were obtained from the three strain gauges on the coupon (ε_1 is the strain from the strain gauge on the outer surface of the coupon; ε_2 and ε_3 are the strains from the two strain gauges on the inner surface of the coupon). It is obvious that the curves from the three strain gauges exhibit a two-stage behavior. During the early stage of loading, tensile and compressive strains developed on the inner and outer surfaces respectively due to the dominant bending deformation. As the deformation of the curved coupon increased (namely as the curvature of the coupon decreased), the loading process entered the second stage where the stress increases approximately linearly with respect to strains on both the inner and the outer surfaces (Figure 3a). During this stage, the membrane deformation starts to dominate the response. The tensile stress-average tensile strain curve, where the average tensile strain ε_{ave} was averaged from the two surface strains [i.e., the average of ε_1 and $\left(\varepsilon_2+\varepsilon_3\right)/2$], is also shown in the figure. It is evident that this curve is almost linear over the full range of loading except the very beginning of the loading process, which can be used to obtain the elastic modulus of the FRP coupon. Figure 3b shows that the tensile stress-average tensile strain curves of all the five coupons are close to each other and all exhibit a linear response after the axial strain exceeds around 0.0004. The linear behavior of the coupons is mainly attributable to the fibers being close to the hoop direction (± 81° to the longitudinal axis) of the FRP tubes [30]. The slightly nonlinear initial portion may be a result of slips of the coupon at both ends into tight contact with the clamping fixtures during the initial loading stage. This nonlinear initial portion was excluded in calculating the elastic modulus of the FRP coupons. Instead, the linear portions with axial strains ranging from 0.001 to 0.004 were used, leading to an average elastic modulus of 35.4 GPa for the tubes. It should be noted that the coupons were not tested to rupture due to the slips between the coupon and the clamping fixtures at a later loading stage, and thus the rupture strains of the FRP tubes were not obtained from the curved coupon tests. It should be noted that due to the large bending strains introduced by the testing process, the rupture strain determined from a curved coupon test is also not representative of that of the FRP tube under hoop tension. The obtained elastic modulus of the 6-ply GFRP tubes was adjusted appropriately to consider the difference in actual fiber volume fraction for the 9-ply GFRP tubes by assuming that each ply of the tubes of different thicknesses carried the same tensile force at a given tensile strain and thus the two tubes had the same value of $E_f t_f/n$, where E_f is the elastic modulus based on the actual thickness t_f and n is the number of plies of the FRP tube. It should be noted that the above treatment ignores the contribution from the resin, which led to a slightly underestimated value for the elastic modulus of the 9-ply GFRP tubes.

Axial compression tests on five GFRP rings with a height of 60 mm cut from a 6-ply GFRP tube were also carried out to obtain the axial properties of the GFRP tubes in accordance with GB/T5350-2005 [31] (Figure 4). Before the compression test, each of the two ends of the FRP ring was strengthened by wrapping a 15 mm wide carbon FRP (CFRP) strip on both the inner and outer surfaces to avoid local failure at the ends (Figure 4a). Four 10-mm axial strain gauges and four 10-mm hoop strain gauges were installed at 90 degrees apart on the outer surface of the FRP ring at the mid-height. Displacement control was used (rate = 0.036 mm/min) in the compression tests. Figure 4c shows the axial stress-axial strain curves of the five FRP rings. The average ultimate axial stress and ultimate axial strain were 79.3 MPa and 1.1%, respectively. The average elastic modulus measured between axial strains of 0 and 0.005, which generally represents the initial elastic behavior of the tubes, was 9.1 GPa [27].

2.3. Preparation of Specimens

All the RCLs were placed in water for 24 hours before being mixed with fresh concrete (Figure 5a). The surfaces of all the RCLs were dried using dry towels before casting so that the water-cement ratio of the fresh concrete was not affected. The GFRP tubes were used directly as molds for casting concrete. The GFRP tube was first fixed on a wooden plate using steel rods (Figure 5b). Fresh concrete was then added to form a thin base layer at the bottom of the tube. RCLs and fresh concrete were then alternately poured into the tube. Meanwhile, the tube was put on a vibration table to guarantee the compaction of compound concrete. All the specimens were cured in the laboratory environment for at least 28 days. Before the compression test, each column was strengthened with a 30 mm wide CFRP strip at each end to avoid undesired local failure at the ends (Figure 5c). For the unconfined specimens, PVC tubes instead of GFRP tubes were used as molds for concrete casting. The PVC tubes were removed from the specimens after curing for 28 days at room temperature.

2.4. Test Set-Up and Instrumentation

For each CCFFT specimen, eight 20-mm strain gauges were evenly distributed around the circumference of the mid-height section to measure the hoop strains, and four 100-mm axial strain gauges at 90 degrees apart were installed to measure the axial strains (Figure 6a). Two linear variable displacement transducers (LVDTs) were installed at 180 degrees apart covering a mid-height region of 210 mm (referred to as the mid-height LVDTs hereafter) to measure the axial shortenings of the specimens (Figure 6a). In addition, four LVDTs were used to measure the total axial shortenings (referred to as the full-height LVDTs hereafter). For each unconfined column, four 50-mm hoop strain gauges and four 100-mm axial strain gauges were installed at 90 degrees apart at the column mid-height to measure the hoop strains and the axial strains, respectively. The number and arrangement of LVDTs were the same as those used for the CCFFT specimens. All the specimens were tested on a large testing machine with a load capacity of 10000 kN (Figure 6b). Loading was applied via displacement control with a rate of 0.24mm/min for all the specimens. All test data, including the loads, strains, and displacements, were simultaneously recorded by a data logger.

2.5. Loading Schemes

Two cyclic loading schemes were employed: Type C1 and Type C2. Full unloading/reloading cycles were used in both loading schemes, which means that the unloading path of each cycle reaches the zero-stress axis, and the reloading path reaches the previous unloading displacement or the envelope curve. For the Type C1 scheme, at each prescribed unloading displacement value, one single full unloading/reloading cycle was applied before the failure of specimen (Figure 7a). For the Type C2 scheme, at a given prescribed unloading displacement value, several repeated internal unloading/reloading cycles were applied on the specimen (Figure 7b). The prescribed unloading displacement values for each test specimen are listed in Table 2. The displacement values averaged from the four full-height LVDTs were used to control the process of unloading/reloading of each specimen.

3. Test Results and Discussions

3.1. General Observations

All the CCFFT specimens failed by the rupture of the FRP tube due to hoop tension in a region away from the two column ends, and the rupture failure generally involve the column mid-height region (Figure 8). The failure processes of all the CCFFT specimens were similar. The presence of RCLs or the type of loading scheme did not seem to have an obvious effect on the failure modes of the test specimens. FRP tube damage was first revealed by the appearance of some white patches on the FRP tube along the fiber directions. This generally occurred when the axial strain exceeded the axial strain at peak stress of unconfined concrete (ε_{co}). As the loading process continued, the white patches expanded, which was accompanied by continuous snapping sounds. Finally, abrupt rupture of fibers occurred with an explosive sound indicating the attainment of the ultimate state of the specimen.

3.2. Axial Strains and Hoop Strains

The axial strains of a test specimen can be obtained from the following three methods of measurement: (1) the average readings from the four full-height LVDTs (referred to as nominal axial strains); (2) the average readings from the two mid-height LVDTs (referred to as LVDT-210 axial strains); (3) the average readings from the four axial strain gauges at the column mid-height (referred to as SG-100 axial strains). It was found that the LVDT-210 axial strain was close to the SG-100 axial strain throughout the loading process for all the test specimens. For specimens with a 6-ply FRP tube, the nominal axial strain was close to the other two axial strains only during the early loading stage (when the axial strain was smaller than around 0.005), after which the nominal axial strain became significantly larger than the other two axial strains. The same observation was reported in Zhang et al. [27] for normal concrete-filled FRP tubular columns. This observation implies that large localized deformations occurred outside the mid-height 210 mm region covered by the mid-height LVDTs. The possible slips between the GFRP tube and the concrete may also be responsible for some of the above discrepancy in the axial strain. As a result, the nominal axial strain is a more reasonable representation of the average deformation of the entire column and is thus used in the subsequent discussions of the present paper. For the test specimens with a thicker GFRP tube (i.e., 9-ply FRP tube), however, the axial strains obtained from the three methods were close to each other throughout the loading process, indicating a more uniform deformation of concrete over the column height due to a stronger FRP confinement. Table 3 lists the key test results, including the peak axial stresses (f_{cc}) and the corresponding nominal axial strains (ε_{cc}), the ultimate nominal axial strains at FRP rupture (ε_{cu}) and the corresponding axial stresses (f_{cu}), and the average FRP hoop rupture strains ($\varepsilon_{h,rup}$) of all the test specimens. Tensile stresses/strains in the FRP tubes are taken to be positive while compressive stresses/strains in the concrete are taken to be positive in the present paper unless otherwise specified.

3.3. Stress-Strain Curves of Concrete

The axial stress-axial strain (nominal axial strain) curves of concrete in the specimens under monotonic compression are shown in Figure 9. The axial stress was obtained from the axial load carried by the concrete divided by the concrete cross-sectional area. The axial load carried by the concrete core in a CCFFT specimen was determined by deducting the axial load carried by the GFRP tube from the total axial load carried by the specimen. The axial load carried by the GFRP tube was obtained using the results of compression tests on hollow GFRP rings (short hollow FRP tubes). The ultimate axial strains of hollow GFRP rings, however, were generally much smaller than those of the CCFFT specimens. As the FRP tube receives support from the concrete core, it is assumed that the load resisted by the GFRP tube in a CCFFT specimen remained constant beyond the ultimate axial strain determined from the GFRP rings [27]. Furthermore, during unloading/reloading, the load resisted by the GFRP tube is assumed to change proportionally to the total load acting on the specimen (thus, the load carried by the GFRP tube becomes zero when the total load reduces to zero) [27].

Figure 9 shows the effects of RCLs and FRP tube thickness on the monotonic stress-strain behavior of concrete. The stress-strain curve of specimen C90-R0-T6-M without RCLs exhibits a descending second portion after the peak stress followed by an ascending third portion, which indicates that the confinement provided by a 6-ply FRP tube was insufficient to ensure a typical monotonically increasing bilinear stress-strain curve for the FRP-confined concrete in this case. The inclusion of RCLs led to obviously different stress-strain curves as indicated by the results for specimens C90-R15-T6-M and C90-R30-T6-M: the axial stresses during and after the transition region are significantly reduced due to the presence of RCLs. This is different from the observation made in a previous study by the authors that the inclusion of RCLs did not have an obvious effect on the stress-strain curve of FRP-confined compound concrete [21]. Note that the RCLs had a compressive strength smaller than that of the fresh concrete in both studies. The difference between these two studies lies in the fact that the specimens in Zhou et al. [21] were provided with a sufficiently large confinement which allowed the corresponding FRP-confined concrete without RCLs to exhibit a monotonically increasing bilinear stress-strain curve, while in the present study, the confinement provided by a 6-ply GFRP tube was insufficient to ensure such behavior as shown by the curve of specimen C90-R0-T6-M in Figure 9. It may thus be concluded that the detrimental effect associated with the use of RCLs can be eliminated only when the compound concrete is provided with a sufficiently large confinement. The quantification of such a threshold confinement, however, requires further studies in the future. When a thicker GFRP tube with 9 plies was used, the resulting stress-strain curve of the FRP-confined compound concrete (C90-R30-T9-M) exhibits an obviously bilinear shape. The axial stresses after the transition region remain at a high level (close to the fresh concrete strength of 90.0 MPa after the transition region), which means that the detrimental effect of RCLs seems to have been largely eliminated by the confinement of a 9-ply FRP tube.

The stress-strain curves of concrete in all the specimens are shown in Figure 10. The curves of the specimens under cyclic axial compression are compared with those of the corresponding specimens under monotonic axial compression. It is evident that the envelope curve of the specimen under cyclic axial compression is close to the curve of the corresponding specimen under monotonic axial compression. The figure also shows that the cyclic stress-strain curves of FRP-confined compound concrete possess the following key characteristics similar to those of FRP-confined normal concrete [25,27]: (1) the unloading curve is nonlinear, whereas the reloading curve is almost linear; (2) during the unloading process, the slope of the unloading path decreases as the load reduces; (3) the plastic strain at the end of each unloading path is dependent on the unloading stress/strain; (4) the plastic strain and the stress deterioration is dependent on the loading history.

3.4. Effect of RCLs

The effect of RCLs on the cyclic stress-strain behavior of FRP-confined compound concrete can be investigated by examining two key parameters: (1) plastic strain (ε_{pl}) when an unloading path intersects the strain axis at a zero-stress point under the Type C1 loading scheme; and (2) strain recovery ratio (ω_n) under the Type C2 loading scheme which is defined by the following equation:

$$\omega_n = \frac{\varepsilon_{un,n} - \varepsilon_{pl,n}}{\varepsilon_{un,n} - \varepsilon_{pl,n-1}} \quad (n \geq 2) \tag{1}$$

where $\varepsilon_{pl,n}$ and $\varepsilon_{un,n}$ are the plastic strain and the unloading strain of the *n*th internal unloading/reloading cycle, respectively.

The plastic strain ε_{pl} has been found to be a function of the envelope unloading strain $\varepsilon_{un,env}$ [25,28]. Figure 11 shows the plastic strain versus the envelope unloading strain for three specimens with different RCL mix ratios. A clear proportional relationship between the two parameters can be identified in the figure. The inclusion of RCLs seems to produce only a marginal effect on the relationship. Figure 12 shows the relationship between the strain recovery ratio and the number of full cycles for the same three specimens with different RCL mix ratios. Despite the scatters in the strain recovery ratios of the three specimens, the inclusion of RCLs does not seem to have a clear effect on the relationship between the two parameters. It may thus be concluded that the inclusion of RCLs does not significantly affect the cyclic stress-strain behavior of FRP-confined compound concrete subjected to either the Type C1 or the Type C2 loading scheme.

4. Comparison with Existing Stress-Strain Models

4.1. Monotonic Stress-Strain Curves

The experimental stress-strain curves of specimens under monotonic axial compression are compared with the curves predicted using Jiang and Teng's model [32] previously developed for FRP-confined normal concrete (Figure 13). Jiang and Teng's model [32] has been demonstrated to be among the most accurate analysis-oriented stress-strain models for FRP-confined normal concrete [33-34]. In making the predictions, the compound concrete containing RCLs was first assumed to be homogenous and have a compressive strength equal to that of the fresh concrete (denoted by $f'_{c,fc}$) as suggested by Zhou et al. [21]. The predicted stress-strain curves are terminated when the average FRP hoop rupture strain measured in the column test is reached.

Figure 13a shows that, for the specimen without RCLs (C90-R0-T6-M), the predicted curves agree reasonably well with the test curves, especially for the initial peak axial stress and the ultimate axial strain. However, the axial stresses of specimen C90-R30-T6-M with an RCL mix ratio of 30% are significantly overestimated by Jiang and Teng's model [32] (Figure 13b). As discussed in the preceding sections, the 6-ply GFRP tube in this case did not provide a sufficiently large confinement to the compound concrete and the negative effect of RCLs could not be eliminated. However, for the specimen with the same RCL mix ratio but with a stiffer FRP tube with 9 plies (i.e., C90-R30-T9-M), the predicted curves agree much better with the test curves, although the axial stresses in the transitional region are overestimated by the model as shown in Figure 13c [11,21]. For specimen C90-R30-T6-M, if the compressive strength of the corresponding unconfined compound concrete (i.e., the compressive strength of specimen C90-R30-T0-M) (denoted by $f'_{c,ucc}$) is used in making predictions with Jiang and Teng's model [32], the predicted curves agree much better with the test curves, especially in the transition region (Figure 12b). The peak axial stress and the ultimate axial strain, however, are still overestimated due to the negative effect of RCLs on the ultimate condition of compound concrete under weak confinement. For specimen C90-R30-T9-M, however, the predicted curves using $f'_{c,ucc}$ are much lower than the test curves as shown in Figure 13c.

Figure 13 also shows that the initial slopes of the predicted stress-strain curves are generally larger than the experimental values. This is believed to be caused by the use of nominal axial strains from the full-height LVDTs in generating the experimental stress-strain curves. As discussed earlier, the nominal axial strain is slightly larger than that recorded at the mid-height of the specimen during the initial loading stage. It was found that, when the mid-height axial strains were used, the predicted initial slopes agreed better with the test results. A similar observation was reported by Zhang et al. [27] for FRP-confined normal concrete.

4.2. Cyclic Stress-Strain Curves

The stress-strain curves of FRP-confined compound concrete in the test specimens under cyclic compression are compared with two existing cyclic stress-strain models for FRP-confined normal concrete, namely, Lam and Teng's model [25] and Yu et al.'s model [28]. Lam and Teng's model [25] was originally developed for normal-strength concrete confined with an FRP wrap formed via the wet lay-up process. Yu et al. [28] later refined Lam and Teng's model [25] to arrive at a unified cyclic stress-strain model applicable to both normal-strength concrete and high-strength concrete confined with either an FRP tube or an FRP wrap by making use of a database containing test results of both concrete filled FRP tubes and concrete cylinders confined with an FRP wrap. For the former, the axial load carried by the FRP tube should be deducted from the total axial load in calculating the axial stress of confined concrete as mentioned in Section 3.3, while the axial load carried by the FRP wrap in the latter is negligibly small and can be ignored. Lam and Teng's model [25] has been found to be more accurate than other existing models in predicting the cyclic stress-strain behavior of normal-strength concrete confined with an FRP wrap [26] and Yu et al.'s model [28] was modified from Lam and Teng's model [25]. As a result, these two models are included in the comparison of the present study and they are briefly reviewed in this section, followed by comparisons between their predictions and the experimental results. While there have been some other recent cyclic stress-strain models for FRP-confined concrete (e.g. [35-38]), they were not specifically developed for high-strength concrete and thus were not included in the comparison of the present study.

4.2.1. Lam and Teng's model [25]

The unloading curves in Lam and Teng's model [25] are divided into two types: (1) envelope unloading where the unloading path starts from the envelope curve; and (2) internal unloading where the previous reloading process terminates before reaching the envelope curve. The unloading path of the Type C1 loading scheme in the present experimental program belongs to the first type of unloading, while the unloading path, except for the first unloading path, of the Type C2 loading scheme belongs to the second type of unloading in Lam and Teng's model [25]. For both types of unloading, the unloading path is depicted by the following nonlinear equation:

$$\sigma_c = a\varepsilon_c^{\eta} + b\varepsilon_c + c \tag{2}$$

where ε_c and σ_c = axial strain and axial stress of confined concrete, respectively; η is an exponent controlling the shape of the unloading path; and *a*, *b*, *c* are constants defined by:

$$a = \frac{\sigma_{un} - E_{un,0}(\varepsilon_{un} - \varepsilon_{pl})}{\varepsilon_{un}^{\eta} - \varepsilon_{pl}^{\eta} - \eta\varepsilon_{pl}^{\eta-1}(\varepsilon_{un} - \varepsilon_{pl})} \tag{3}$$

$$b = E_{un.0} - a\eta\varepsilon_{pl}^{\eta-1} \tag{4}$$

$$c = -a\varepsilon_{pl}^{\eta} - b\varepsilon_{pl} \tag{5}$$

where σ_{un} and ε_{un} = unloading stress and strain at the initiation of unloading, respectively; and $E_{un,0}$ = slope of unloading path at zero-stress. Both η and $E_{un,0}$ are a function of the unloading strain:

$$\eta = 350\varepsilon_{un} + 3 \tag{6}$$

$$E_{un.0} = \min\left(\frac{0.5 f'_{co}}{\varepsilon_{un}}, \frac{\sigma_{un}}{\varepsilon_{un} - \varepsilon_{pl}}\right) \tag{7}$$

For envelope unloading (the Type C1 loading scheme), the plastic strain is given as a function of the concrete strength f'_{co} and the envelope unloading strain $\varepsilon_{un,env}$:

$$\varepsilon_{pl,1} = \begin{cases} 0 & 0 < \varepsilon_{un,env} \le 0.001 \\ \left[1.4(0.87 - 0.004 f'_{co}) - 0.64\right](\varepsilon_{un,env} - 0.001) & 0.001 < \varepsilon_{un,env} < 0.0035 \\ (0.87 - 0.004 f'_{co})\varepsilon_{un,env} - 0.0016 & 0.0035 \le \varepsilon_{un,env} \le \varepsilon_{cu} \end{cases} \tag{8}$$

For internal unloading (the Type C2 loading scheme), the plastic strain is calculated from the following equations of the strain recovery ratio ω_n in combination with Eq. (1):

$$\omega_n(2 \le n \le 5) = \begin{cases} 1 & 0 < \varepsilon_{un,env} \le 0.001 \\ 1 + 400(0.0212n - 0.12)(\varepsilon_{un,env} - 0.001) & 0.001 < \varepsilon_{un,env} < 0.0035 \\ 0.0212n + 0.88 & 0.0035 \le \varepsilon_{un,env} \le \varepsilon_{cu} \end{cases} \tag{9a}$$

$$\omega_n(n \ge 6) = 1 \tag{9b}$$

where $\varepsilon_{pl,n}$, $\varepsilon_{un,n}$, and *n* are defined under Eq. (1).

The reloading path of Lam and Teng's model [25] consists of two portions: a linear portion from the reloading point $\left(\varepsilon_{re}, \sigma_{re}\right)$ to the reference point $\left(\varepsilon_{ref}, \sigma_{new}\right)$ and a parabolic portion connecting the reference point to the envelope curve. The reference strain ε_{ref} is equal to the envelope unloading strain $\varepsilon_{un,env}$. The stress at the reference strain is referred to as the new stress σ_{new}, which is smaller than the stress on the previous unloading path due to the stress deterioration effect. The full reloading path is described by the following equation:

$$\sigma_c = \begin{cases} \sigma_{re} + E_{re}(\varepsilon_c - \varepsilon_{re}) & \left(\varepsilon_{re} \le \varepsilon_c \le \varepsilon_{ref}\right) \\ A\varepsilon_c^2 + B\varepsilon_c + C & \left(\varepsilon_{ref} < \varepsilon_c \le \varepsilon_{ret,env}\right) \end{cases} \tag{10}$$

where $E_{re} = (\sigma_{new} - \sigma_{re}) / (\varepsilon_{ref} - \varepsilon_{re})$ is the slope of the linear portion; $\varepsilon_{ret,env}$ is the envelope returning strain where a reloading path meets the envelope curve; and *A*, *B*, *C* are constants to be determined based on the condition that the parabolic portion is connected to the linear reloading path and the envelope curve smoothly. The detailed expressions for *A*, *B*, *C*, as well as the calculation for σ_{new}, can be found in Lam and Teng's model [25].

4.2.2. Yu et al.'s model [28]

The expressions of Eqs. (2) and (10) of Lam and Teng's model [25] were directly adopted by Yu et al. [28] to describe the unloading and reloading paths, respectively, but some revisions were made to the key parameters in these equations. They found that η in Eq. (6) not only depends on the unloading strain but also on the unconfined concrete strength:

$$\eta = 40(350\varepsilon_{un} + 3) / f'_{co} \tag{11}$$

The plastic strain of an envelope unloading (the Type C1 loading scheme) was revised to be independent of the unconfined concrete strength as follows:

$$\varepsilon_{pl,1} = \begin{cases} 0 & 0 < \varepsilon_{un,env} \le 0.001 \\ 0.184\varepsilon_{un,env} - 0.0002 & 0.001 < \varepsilon_{un,env} < 0.0035 \\ 0.703\varepsilon_{un,env} - 0.002 & 0.0035 \le \varepsilon_{un,env} \le \varepsilon_{cu} \end{cases} \tag{12}$$

The equation of the strain recovery ratio ω_n was revised to become:

$$\omega_n(n \ge 2) = \begin{cases} 1 & 0 < \varepsilon_{un,env} \le 0.001 \\ 1 - 32(\varepsilon_{un,env} - 0.001) / (n-1) & 0.001 < \varepsilon_{un,env} \le 0.0035 \\ -0.08 / (n-1) + 1 & 0.0035 < \varepsilon_{un,env} \le \varepsilon_{cu} \end{cases} \tag{13}$$

Other revisions include the equations of stress deterioration ratios to calculate the new stress σ_{new}. The readers are referred to Yu et al. [28] for more details about the revisions.

4.2.3. Comparison with test results

In Figure 11, the results predicted using Lam and Teng's model [25] [Eq. (8)] and Yu et al.'s model [28] [Eq. (12)] respectively for the relationship between the envelope unloading strain and the plastic strain are shown against the experimental results. It is obvious that Eq. (12) of Yu et al.'s model [28] predicts the tests result much better than Eq. (8) of Lam and Teng's model [25] for the three specimens with different RCL mix ratios. Lam and Teng's model [25] significantly underestimates the plastic strains. Figure 12 shows the predictions of the two models [Eqs. (9) and (13)] respectively for the relationship between the strain recovery ratio and the number of full cycles. It is also seen that Yu et al.'s model [28] performs better than Lam and Teng's model [25], especially for the first 4 effective cycles.

Figure 14 shows a comparison of envelope unloading/reloading curves between the predictions from the two models and the test results for specimens under the Type C1 loading scheme. The experimental envelope curves were directly used in making the predictions of the models; therefore, the possible errors from the models in predicting the envelope stress-strain curves can be excluded. Being consistent with Figure 11, it is seen that the plastic strains predicted by Yu et al.'s model [28] agree much better with the experimental results. Nevertheless, Yu et al.'s model [28] predicts larger plastic strains for all loading cycles of specimen C90-R30-T9-C1 confined with a 9-ply GFRP tube (Figure 14d). This observation is consistent with the finding given in Yu et al. [28] that Eq. (12) overestimates the plastic strains for specimens with a relatively high level of FRP confinement.

To exclude the errors of Eqs. (8) and (12) in predicting the plastic strains $\varepsilon_{pl,1}$, another set of predictions using directly the experimental values of $\varepsilon_{pl,1}$ was generated and compared with the experimental cyclic curves in Figure 15. It is interesting to see that now the unloading paths predicted by Lam and Teng's model [25] agree much better with the experimental curves than those predicted by Yu et al.'s model [28], which means that Eq. (6) of Lam and Teng's model [25], which controls the shape of an unloading path, is more accurate than Eq. (11) of Yu et al.'s model [28]. Lam and Teng's model [25] performs well for specimens with different RCL mix ratios (0%, 15%, and 30%), which also implies that the inclusion of RCLs does not have an obvious effect on the cyclic behavior of FRP-confined compound concrete.

The internal unloading/reloading cycles of the specimens under the Type C2 loading scheme are compared with model predictions in Figure 16. Each cycle is shown individually in the figure in a region with a width representing a strain range of 0.01 to avoid the overlapping of internal cycles with the same unloading strain. Only the first, fourth, seventh, and last cycles are shown in the figure for a clear comparison. Again, the experimental unloading strain and unloading stress were directly used in making the predictions so that the comparison only reflects the accuracy of the models in predicting the internal unloading/reloading curves. It is evident from Figure 16 that both models predict reasonably well the unloading/reloading paths of specimens confined with a 6-ply GFRP tube, with Lam and Teng's model [25] being slightly better. For specimen C90-R30-T9-C2 with a 9-ply GFRP tube, Lam and Teng's model [25] performs much better than Yu et al.'s model [28]; the latter overestimates the plastic strains of specimens with a relatively high level of FRP confinement as mentioned earlier.

5. Conclusions

A novel and attractive technique to recycle demolition concrete is to crush old concrete coarsely into concrete lumps (RCLs) for direct mixing with fresh new concrete, leading to what may be referred to as compound concrete. Existing research has revealed a number of performance concerns with such compound concrete, including reductions in the strength and durability of the concrete. Encasement of compound concrete with an FRP tube has recently been explored as an effective option to improve the properties of compound concrete. This paper has presented the results of the first ever experimental study on the behavior of compound concrete filled FRP tubular (CCFFT) columns under cyclic axial compression. The effects of RCL mix ratio and level of FRP confinement (i.e., FRP tube thickness) on the cyclic stress-strain response of FRP-confined compound concrete have been examined. Based on the experimental results and their comparisons with predictions from two stress-strain models, the following observations and conclusions may be made:

1. All the CCFFT columns failed by FRP rupture due to hoop tension; the presence of RCLs or the details of the cyclic loading scheme did not have an obvious effect on the column failure mode.
2. For the CCFFT specimens with a 6-ply FRP tube, the axial stresses in and after the transition region were significantly reduced due to the presence of RCLs; however, for the specimens with a 9-ply FRP tube, the axial stresses after the transition region remained at the expected high level. This observation indicates that the negative effect associated with the use of RCLs can be eliminated only when the compound concrete is provided with a sufficiently strong confinement.
3. For CCFFT columns confined with a stiff FRP tube (e.g., the CCFT specimens with a 9-ply FRP tube in the present study), the predictions of Jiang and Teng's model [32] agree well with the test results if the compressive strength of the compound concrete is assumed to be the same as that of the fresh concrete. However, for the CCFFT columns with a relatively weak confinement (6-ply FRP tube), the compressive strength of the corresponding unconfined compound concrete should be used for a close prediction of the stress-strain curve.
4. The inclusion of RCLs has only a marginal effect on the cyclic stress-strain behavior, including the plastic strain and the strain recovery ratio, of FRP-confined concrete.
5. Yu et al.'s model [28] performs better than Lam and Teng's model [25] in predicting the envelope unloading/reloading curves of FRP-confined compound concrete in CCFFT specimens under the Type C1 loading scheme. Both models provide reasonably accurate predictions for the internal unloading/reloading paths of FRP-confined compound concrete in CCFFT specimens under the Type C2 loading scheme. Yu et al.'s model [28], however, overestimates the plastic strains for CCFFT specimens with a relatively high level of FRP confinement.

6. Data availability statement

Some or all data, models, or code that support the findings of this study are available from the corresponding author upon reasonable request.

7. Author Statement

J.K. Zhou: Methodology, Investigation, Formal analysis, Validation, Writing - original draft
G. Lin: Methodology, Investigation, Supervision, Writing - Review & Editing
J.G. Teng: Conceptualization, Supervision, Writing - Review & Editing, Funding acquisition

8. Acknowledgements

The authors are grateful for the financial support received from the Research Grants Council of the Hong Kong Special Administrative Region (Project Reference Numbers: PolyU 5252/13E and T22-502/18-R).

9. References

[1] Poon CS, Shui Z, Lam, L. Effect of microstructure of ITZ on compressive strength of concrete prepared with recycled aggregates. Construction and Building Materials. 2004;18(6):461-468.

[2] Xiao JZ, Li JB, Zhang C. Mechanical properties of recycled aggregate concrete under uniaxial loading. Cement and Concrete Research. 2005;35(6):1187-1194.

[3] Casuccio M, Torrijos M, Giaccio G, Zerbino R. Failure mechanism of recycled aggregate concrete. Construction and Building Materials. 2008;22(7):1500-1506.

[4] Breccolotti M, Materazzi AL. Structural reliability of eccentrically-loaded sections in RC columns made of recycled aggregate concrete. Engineering Structures. 2010;32(11):3704-3712.

[5] Tam VW, Soomro M, Evangelista ACJ. A review of recycled aggregate in concrete applications (2000–2017). Construction and Building Materials. 2018;172:272-292.

[6] Pacheco J, De Brito J, Chastre C, Evangelista L. Experimental investigation on the variability of the main mechanical properties of concrete produced with coarse recycled concrete aggregates. Construction and Building Materials 2019;201:110-120.

[7] Lu B, Shi CJ, Cao Z, Guo M, Zheng J. Effect of carbonated coarse recycled concrete aggregate on the properties and microstructure of recycled concrete. Journal of Cleaner Production. 2019;233:421-428.

[8] Zhan BJ, Xuan DX, Zeng W, Poon CS. Carbonation treatment of recycled concrete aggregate: Effect on transport properties and steel corrosion of recycled aggregate concrete. Cement and Concrete Composites. 2019;104:103360.

[9] Yang YF, Han LH. Experimental behaviour of recycled aggregate concrete filled steel tubular columns. Journal of Constructional Steel Research. 2006;62(12):1310-1324.

[10] Wu B, Liu QX, Liu W, Xu Z. Primary study on recycled-concrete-segment filled steel tubular members, Earthquake Resistant Engineering and Retrofitting. 2008;30(4):120-124. (in Chinese)

[11] Teng JG, Zhao JL, Yu T, Li LJ, Guo YC. Behavior of FRP-confined compound concrete containing recycled concrete lumps. Journal of Composites for Construction, ASCE. 2015;20(1):04015038.

[12] Wu B, Liu W, Liu QX, Xu Z. Test on axial behavior of reinforced concrete columns filled with demolished concrete segment/lump. Earthquake Resistant Engineering and Retrofitting. 2010;32(3):81-85.

[13] Wu B, Liu C, Wu Y. Compressive behaviors of cylindrical concrete specimens made of demolished concrete blocks and fresh concrete. Construction and Building Materials. 2014;53:118-130.

[14] Wu B, Zhang SY, Yang Y. Compressive behaviors of cubes and cylinders made of normal-strength demolished concrete blocks and high-strength fresh concrete. Construction and Building Materials. 2015;78:342-353.

[15] Wu B, Yu Y, Chen ZP Zhao XY. Shape effect on compressive mechanical properties of compound concrete containing demolished concrete lumps. Construction and Building Materials. 2018;187:50-64.

[16] Wu B, Zhao XY, Zhang JS. Cyclic behavior of thin-walled square steel tubular columns filled with demolished concrete lumps and fresh concrete, Journal of Constructional Steel Research. 2012;77:69-81.

[17] Wu B, Zhao XY, Zhang JS, YangY. Cyclic testing of thin-walled circular steel tubular columns filled with demolished concrete blocks and fresh concrete. Thin-Walled Structures. 2013;66:50-61.

[18] Wu B, Zhang Q, Chen GM. Compressive behavior of thin-walled circular steel tubular

columns filled with steel stirrup-reinforced compound concrete. Engineering Structures. 2018;170:178-195.

[19] Wu B, Lin L, Zhao JX, Yan H. Creep behavior of thin-walled circular steel tubular columns filled with demolished concrete lumps and fresh concrete. Construction and Building Materials. 2018;187:773-790.

[20] Teng JG, Zhao JL, Yu T, Li LJ, Guo YC. Recycling of coarsely-crushed concrete for use in FRP tubular columns. Proceedings of the 1st International Conference on Performance-based and Life-cycle Structural Engineering (PLSE 2012), 5-7 December, Hong Kong, China. 2012.

[21] Zhou JK, Lin G, Teng JG. Stress-strain behavior of FRP-confined concrete containing recycled concrete lumps. Construction and Building Materials. 2021;267: 120915.

[22] Mirmiran A, Shahawy M. Behavior of concrete columns confined by fiber composites. Journal of Structural Engineering, ASCE. 1997;123(5):83-590.

[24] Lam L, Teng JG, Cheung C, Xiao Y. FRP-confined concrete under axial cyclic compression. Cement and Concrete Composites. 2006;28(10):949-958.

[25] Lam L, Teng JG. Stress-strain model for FRP-confined concrete under cyclic axial compression. Engineering Structures. 2009;31(2):308-321.

[26] Ozbakkaloglu T, Akin E. Behavior of FRP-confined normal-and high-strength concrete under cyclic axial compression. Journal of Composites for Construction, ASCE. 2011;16(4):451-463.

[27] Zhang B, Yu T, Teng JG. Behavior of concrete-filled FRP tubes under cyclic axial compression. Journal of Composites for Construction, ASCE. 2015;19:04014060.

[28] Yu T, Zhang B, Teng JG. Unified cyclic stress-strain model for normal and high strength concrete confined with FRP. Engineering Structures. 2015;102:189-201.

[29] BS 812. Testing of Aggregate Part 2: Method of Determination of Density. British Standards Institution. London, U.K. 1995.

[30] Xie P, Lin G, Teng JG, Jiang T. Modelling of concrete-filled filament-wound FRP confining tubes considering nonlinear biaxial tube behavior. Engineering Structures. 2020;218:110762.

[31] GB/T5350-2005. Fiber-Reinforced Thermosetting Plastic Composites Pipe: Determination for Longitudinal Compressive Properties. The Standards Press of China. 2005

[32] Jiang T, Teng JG. Analysis-oriented stress-strain models for FRP-confined concrete. Engineering Structures. 2007;29(11):2968-2986.

[33] Lee CS, Hegemier GA. Model of FRP-confined concrete cylinders in axial compression. Journal of Composites for Construction, ASCE. 2009;13(5):442-454.

[34] Ozbakkaloglu T, Lim JC, Vincent, T. FRP-confined concrete in circular sections: Review and assessment of stress-strain models. Engineering Structures. 2013;49:1068-1088.

[35] Wang Z, Wang D, Smith ST, Lu D. Experimental testing and analytical modeling of CFRP-confined large circular RC columns subjected to cyclic axial compression. Engineering Structures. 2012;40:64-74.

[36] Hany NF, Hantouche EG, Harajli MH. Axial stress-strain model of CFRP-confined concrete under monotonic and cyclic loading. Journal of Composites for Construction, ASCE. 2015;19(6):04015004.

[37] Li P, Wu YF. (2015). Stress-strain model of FRP confined concrete under cyclic loading. Composite Structures. 2015;134:60-71.

[38] Li P, Wu YF, Zhou Y, Xing F. Cyclic stress-strain model for FRP-confined concrete considering post-peak softening. Composite Structures. 2018;201:902-915.

Figure 1. Recycled concrete lumps (RCLs)

(a) Curved coupons (b) A coupon under tension

Figure 2. Tensile tests on curved coupons

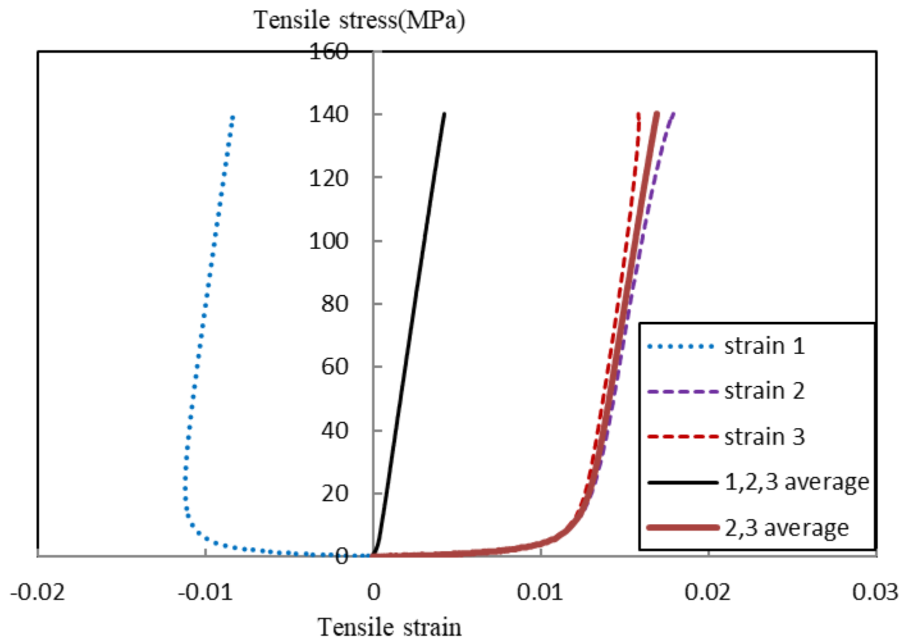

(a) Typical stress-strain curves from three strain gauges on a curved coupon

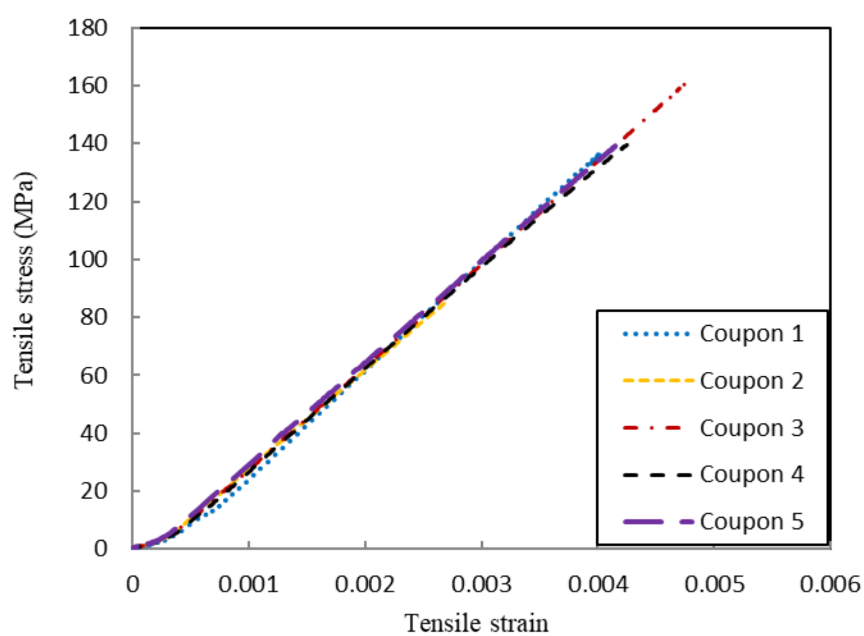

(b) Average stress-strain curves of five coupons

Figure 3. Tensile stress-strain curves of GFRP curved coupons

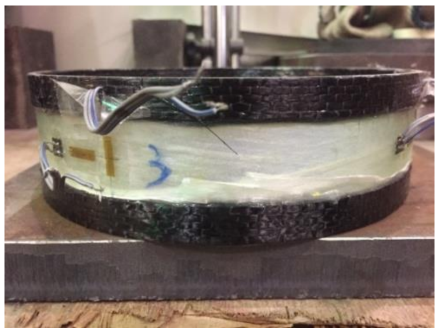 

(a) Test specimen (b) Test setup

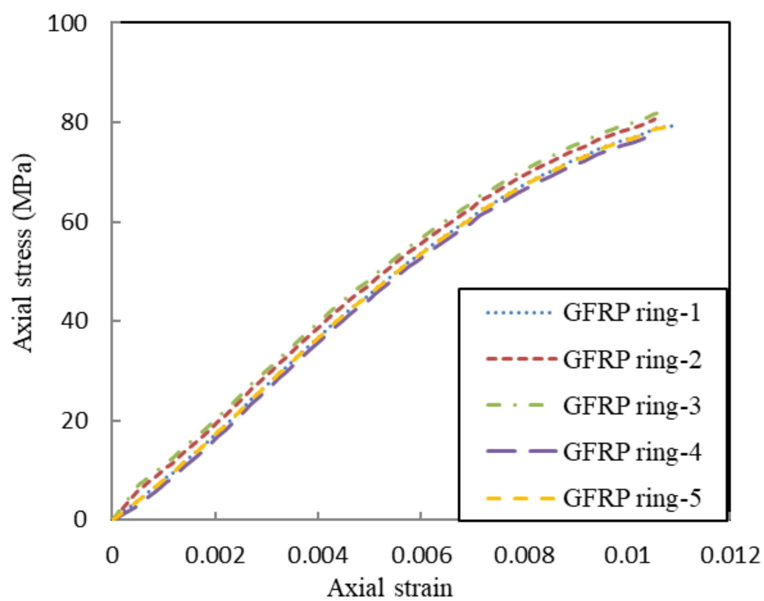

(c) Axial stress-axial strain curves

Figure 4. Compression tests on GFRP rings

(a) RCLs submerged in water (b) FRP tubes

(c) End strengthening with CFRP strips

Figure 5. Fabrication of FRP-confined concrete specimens

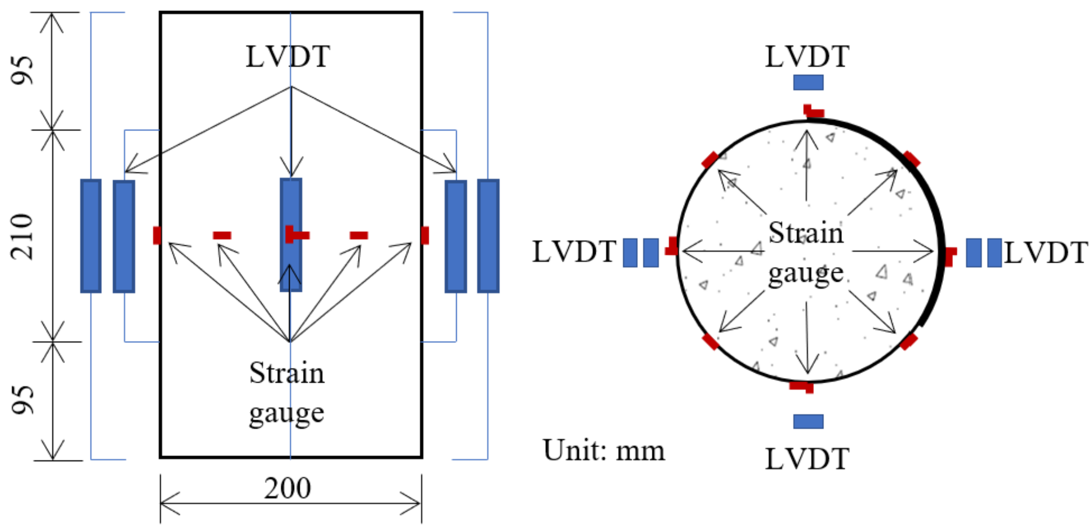

(a) Layout of LVDTs and strain gauges

(b) Test set-up

Figure 6. Test set-up and instrumentation

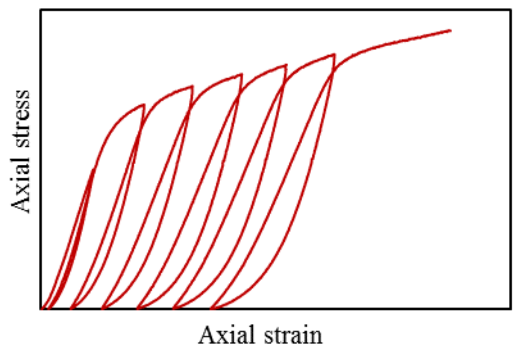

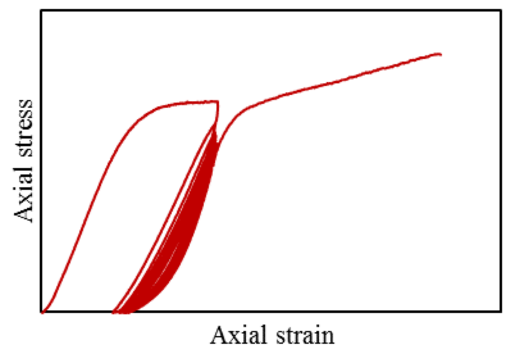

(a) Cyclic loading scheme C1 (b) Cyclic loading scheme C2

Figure 7. Cyclic loading schemes

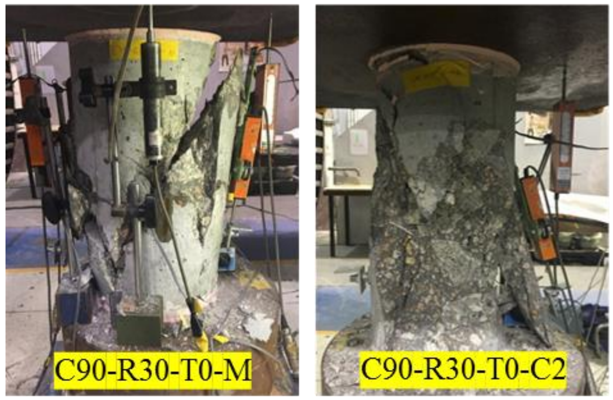

(a) Unconfined specimens

(b) CCFFT specimens (RCL mix ratio = 0%, 6-ply FRP tube)

(c) CCFFT specimens (RCL mix ratio = 15%, 6-ply FRP tube)

(d) CCFFT specimens (RCL mix ratio = 30%, 6-ply FRP tube)

(e) CCFFT specimens (RCL mix ratio = 30%, 9-ply FRP tube)

Figure 8. Specimens after test

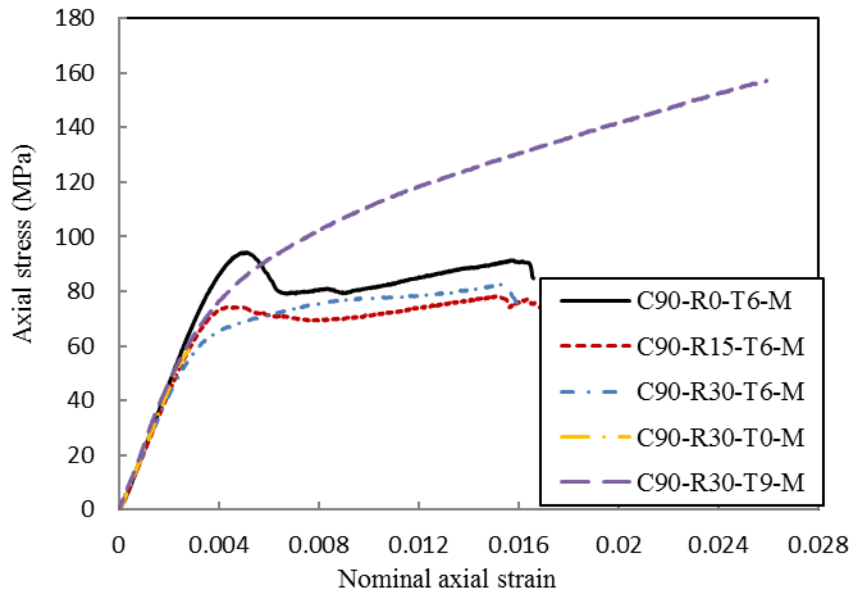

Figure 9. Axial stress-strain curves of specimens under monotonic axial compression

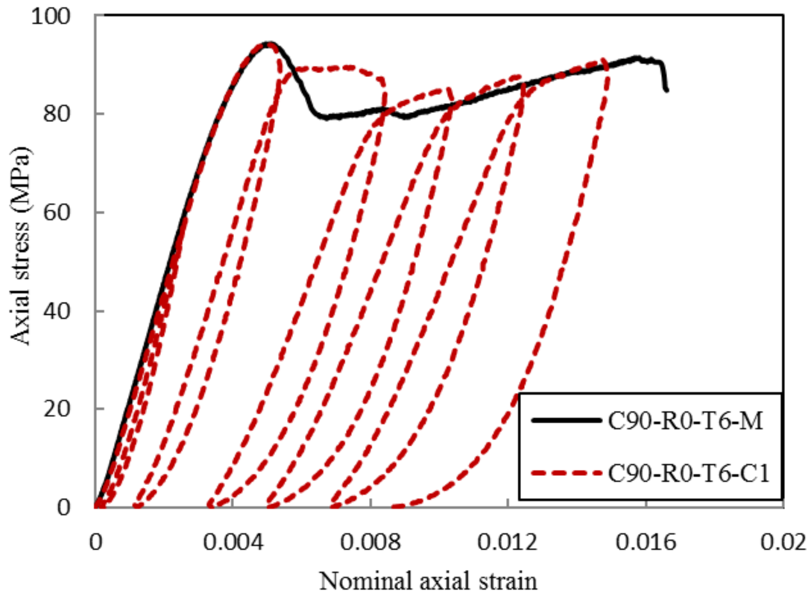

(a) C90-R0-T6-C1

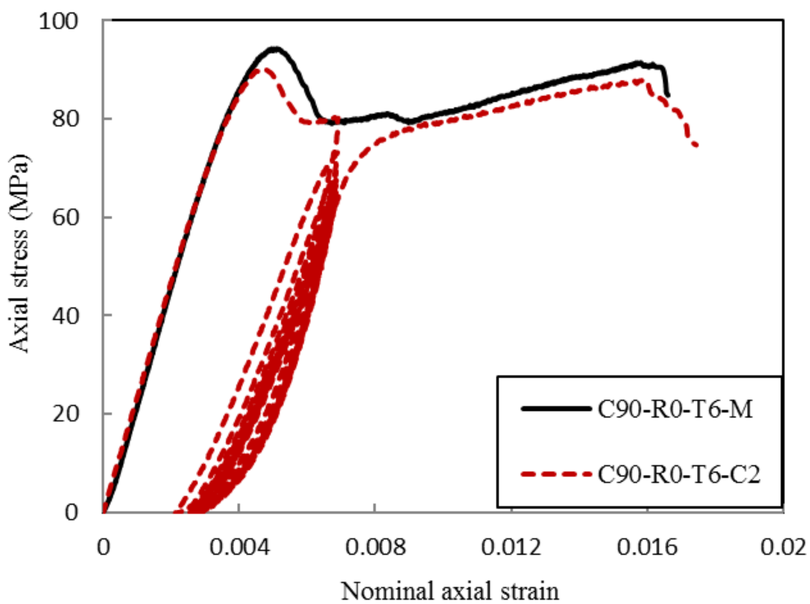

(b) C90-R0-T6-C2

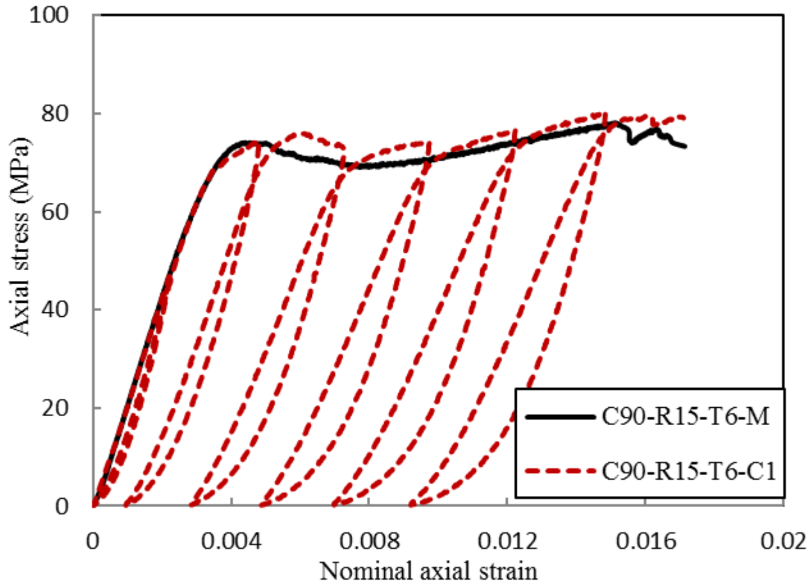

(c) C90-R15-T6-C1

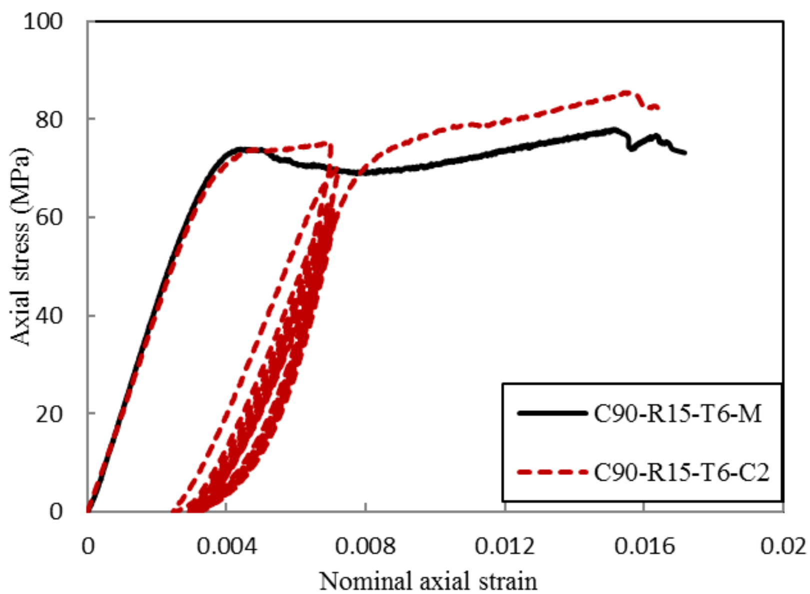

(d) C90-R15-T6-C2

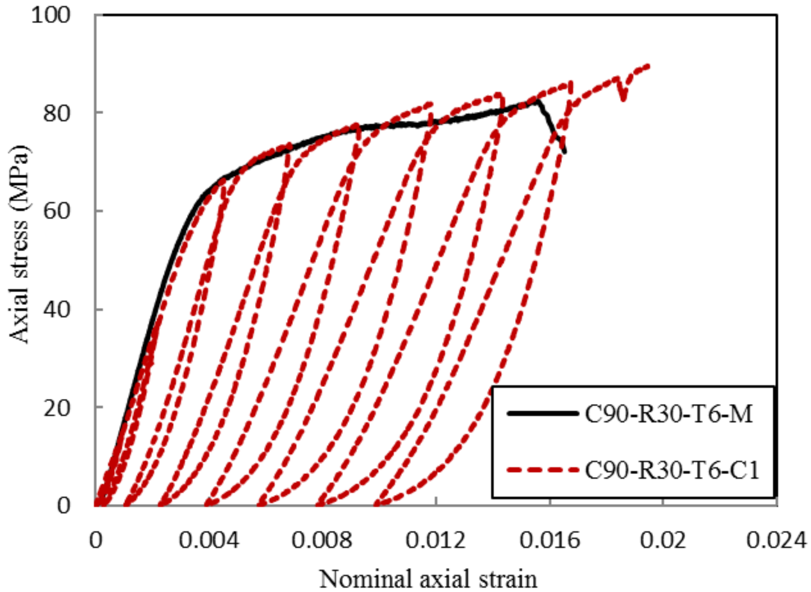

(e) C90-R30-T6-C1

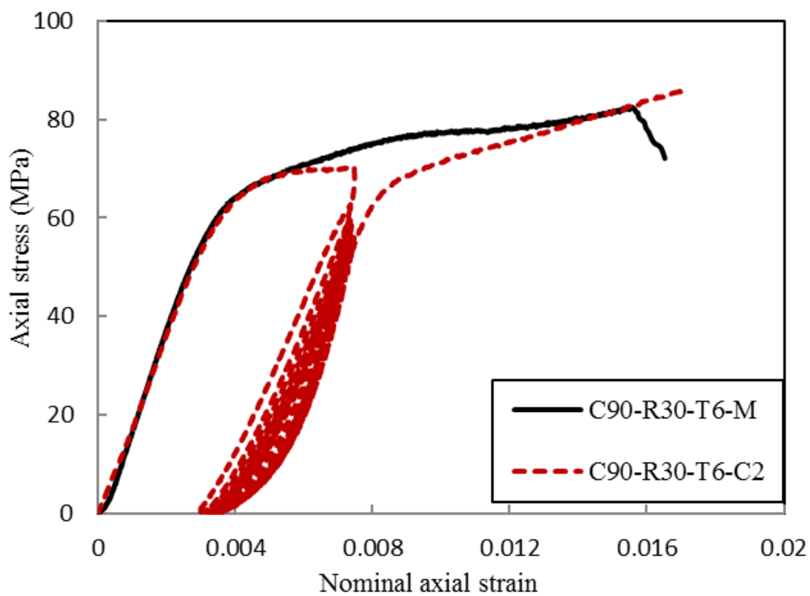

(f) C90-R30-T6-C2

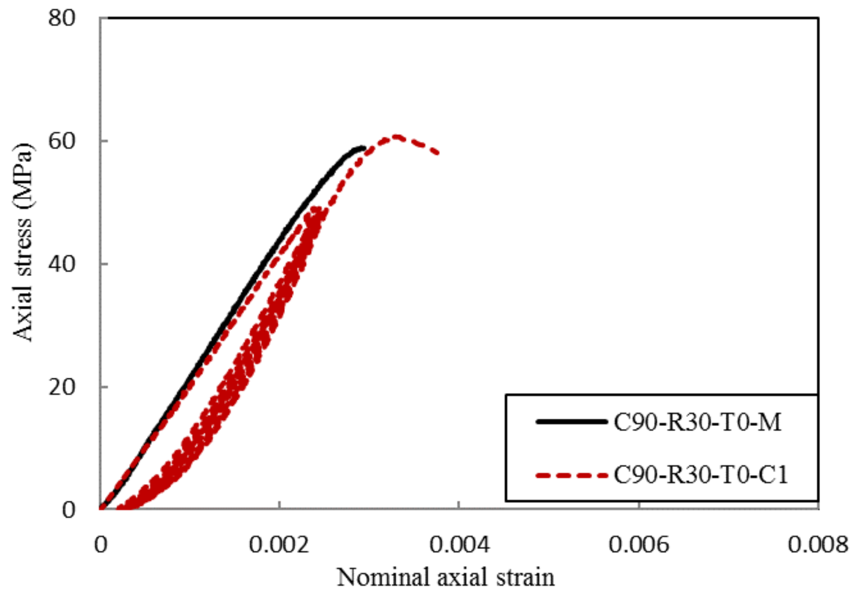

(g) C90-R30-T0-C1

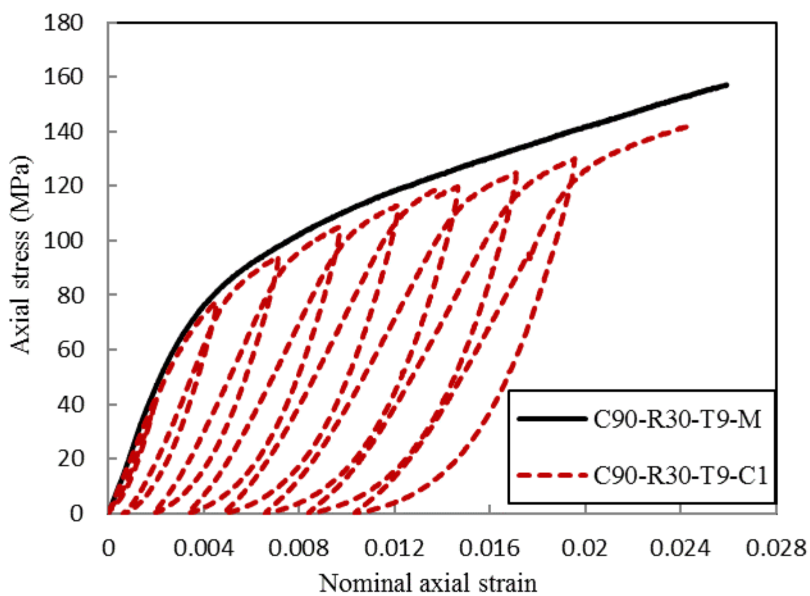

(h) C90-R30-T9-C1

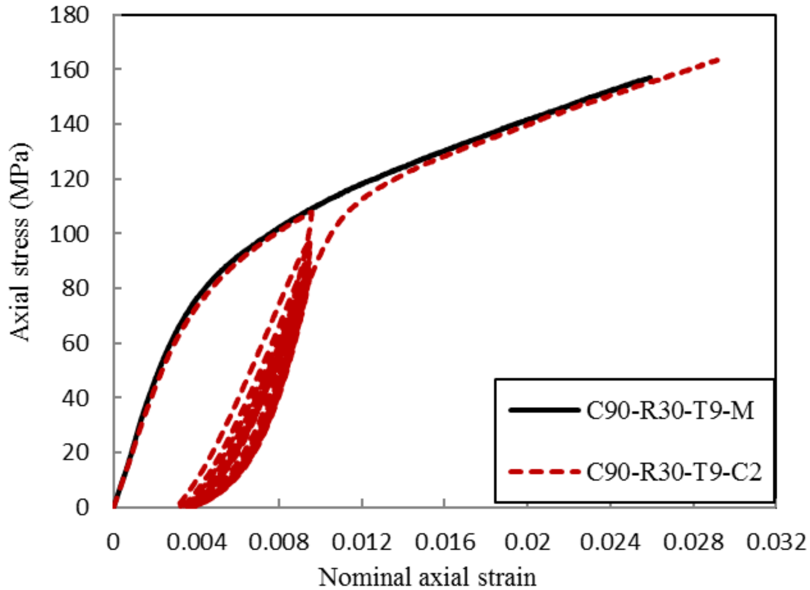

(i) C90-R30-T9-C2

Figure 10. Axial stress-axial strain curves of concrete in all test specimens

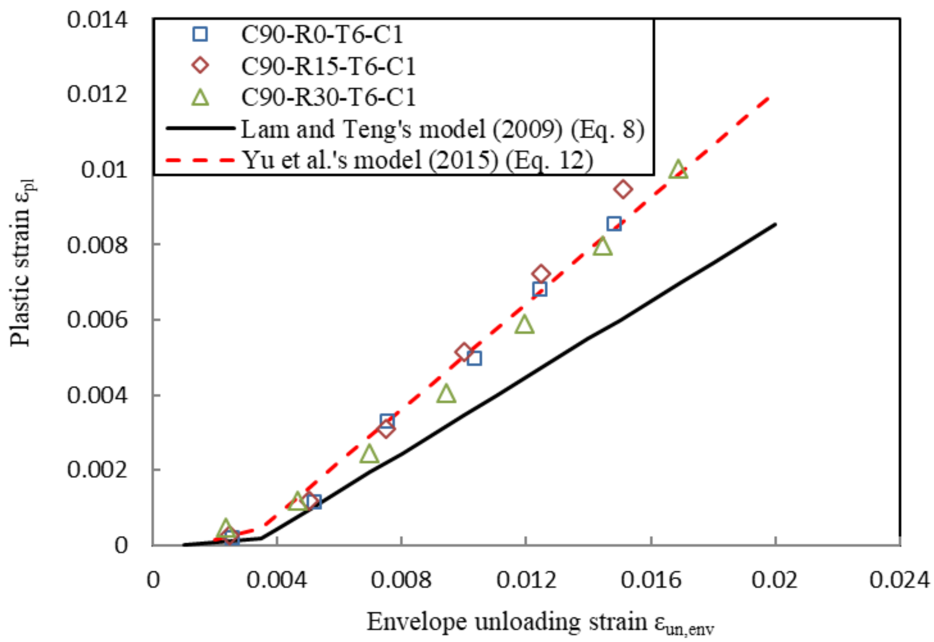

Figure 11. Plastic strain versus envelope unloading strain

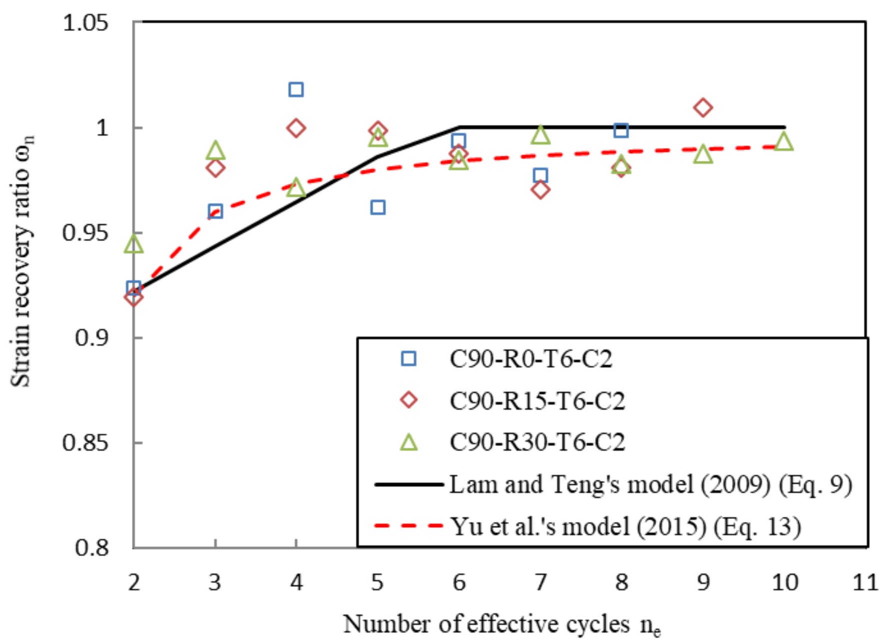

Figure 12. Strain recovery ratio versus number of effective cycles

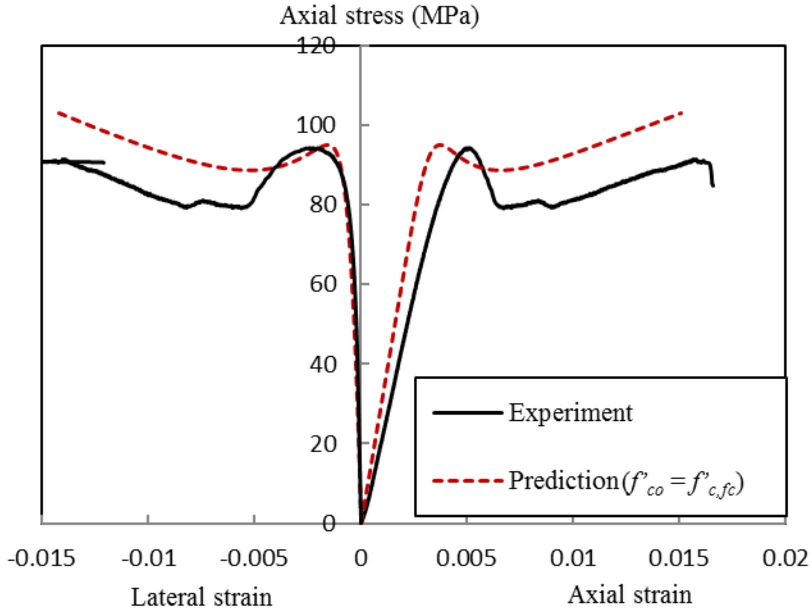

(a) C90-R0-T6-M

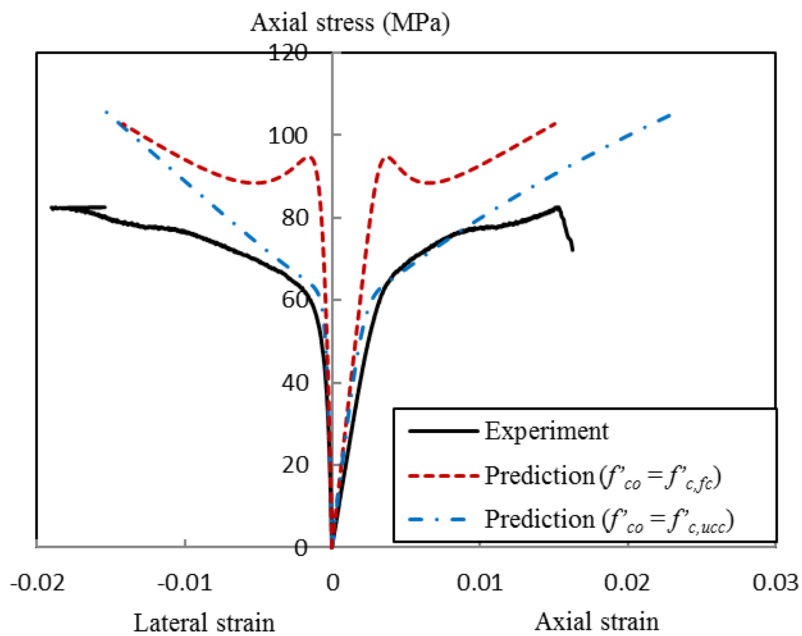

(b) C90-R30-T6-M

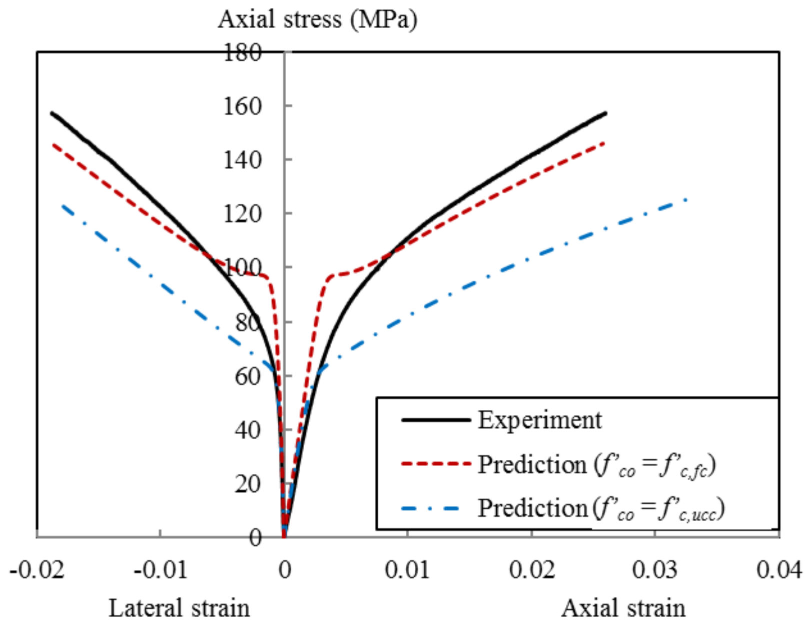

(c) C90-R30-T9-M

Figure 13. Performance of Jiang and Teng's model [32] in predicting monotonic stress-strain curves

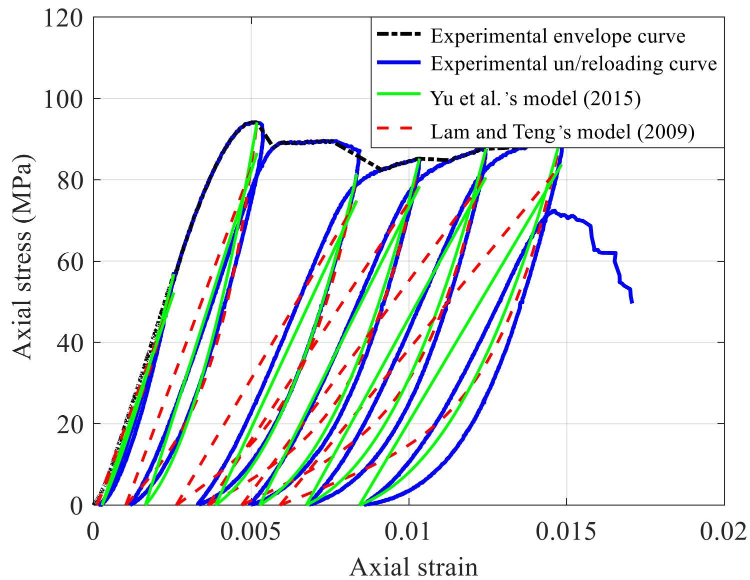

(a) C90-R0-T6-C1

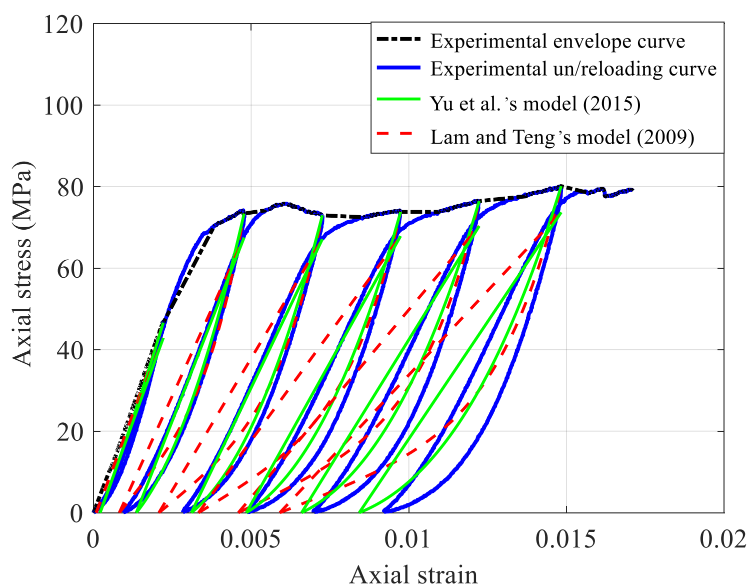

(b) C90-R15-T6-C1

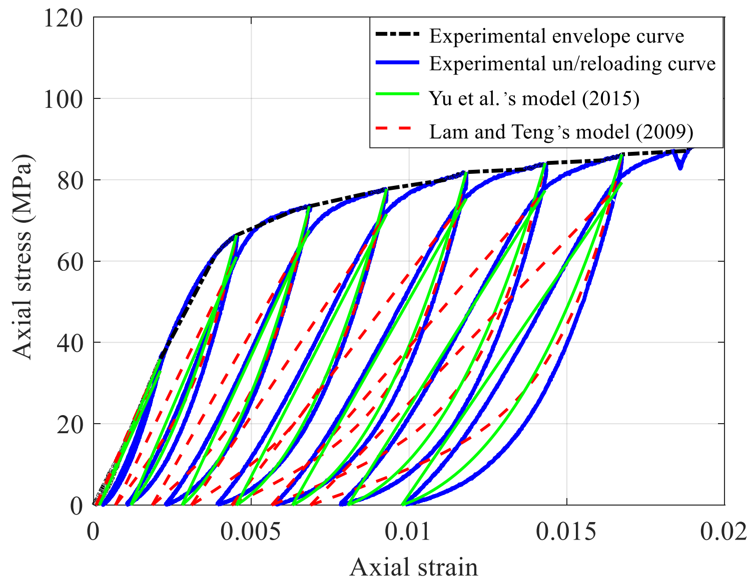

(c) C90-R30-T6-C1

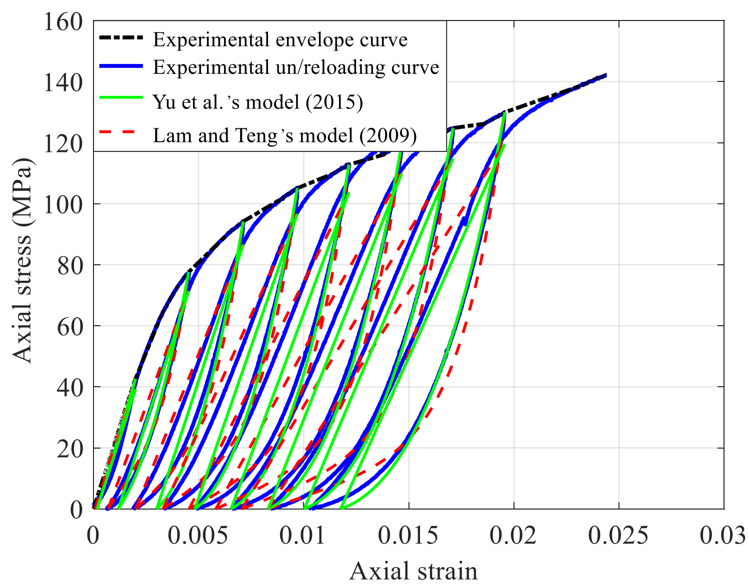

(d) C90-R30-T9-C1

Figure 14. Performance of two models for specimens with Type C1 loading scheme

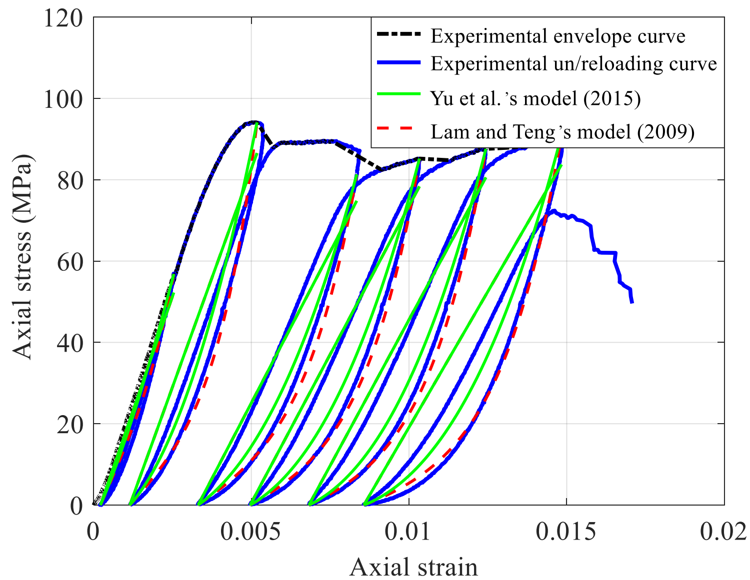

(a) C90-R0-T6-C1

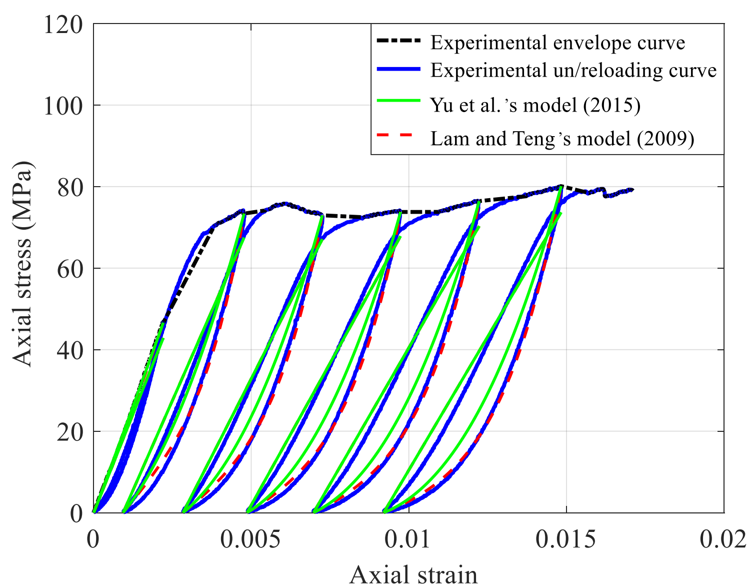

(b) C90-R15-T6-C1

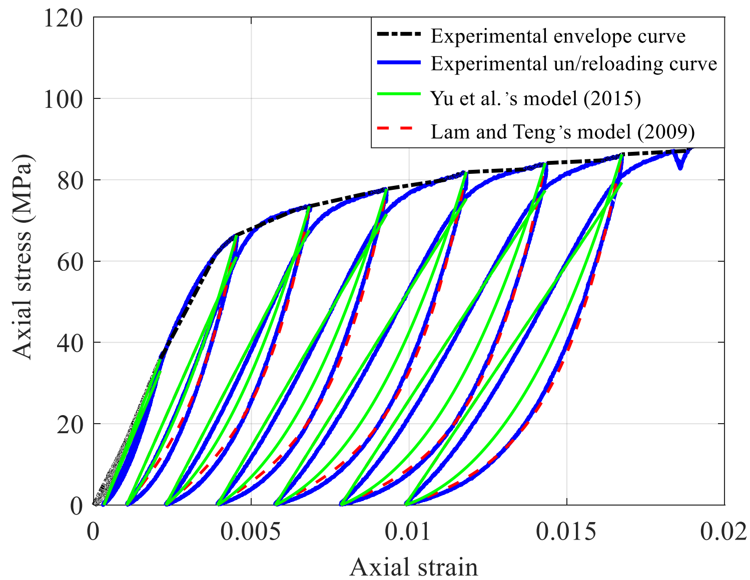

(c) C90-R30-T6-C1

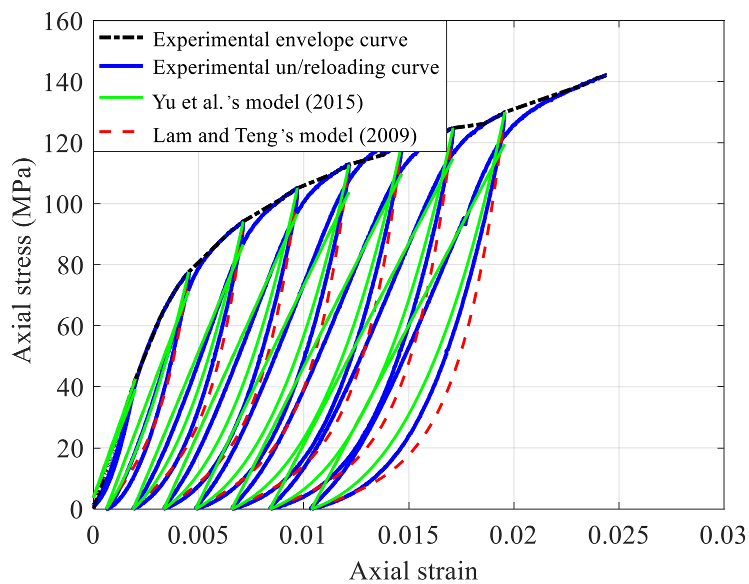

(d) C90-R30-T9-C1

Figure 15. Performance of two models for specimens under Type C1 loading scheme using the experimental value of $\varepsilon_{pl,1}$

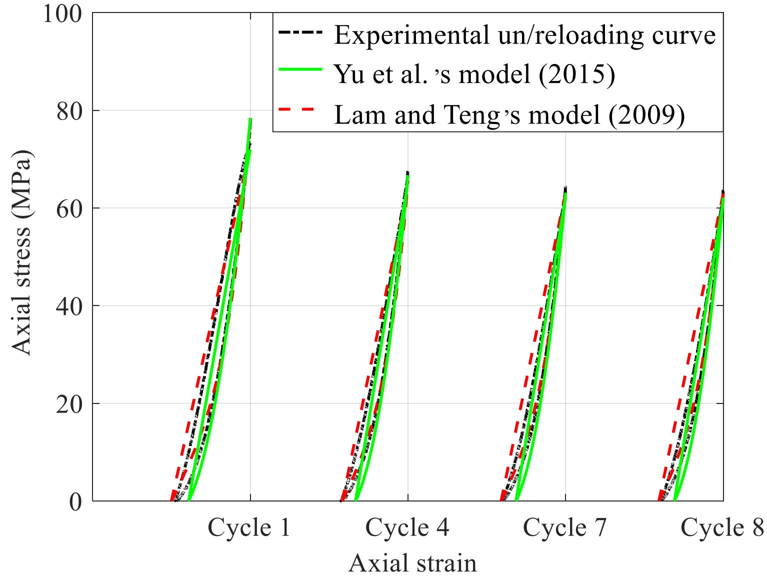

(a) C90-R0-T6-C2

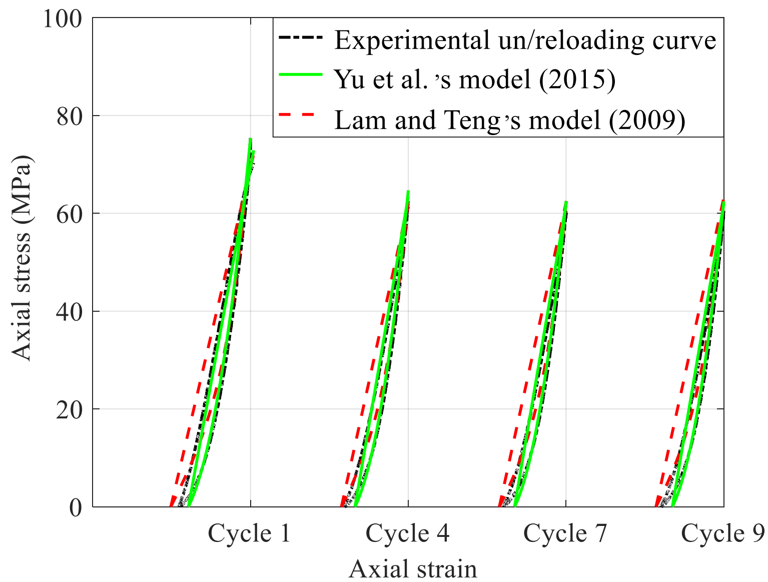

(b) C90-R15-T6-C2

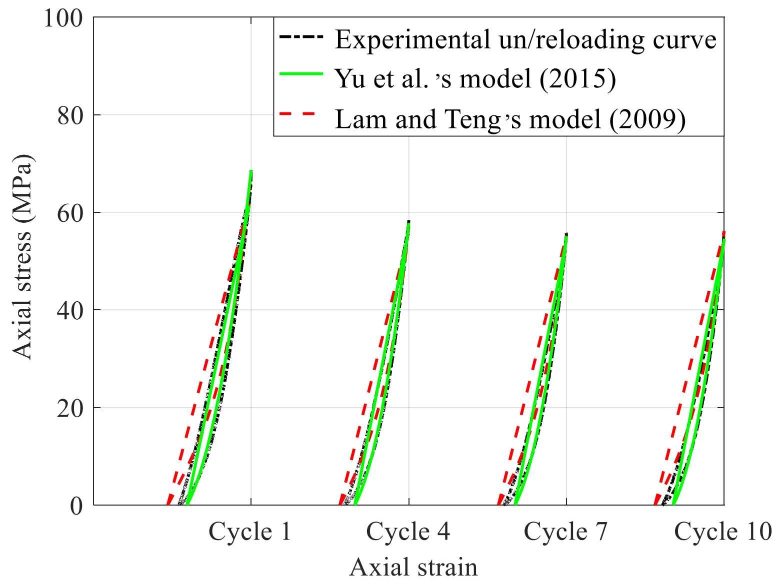

(c) C90-R30-T6-C2

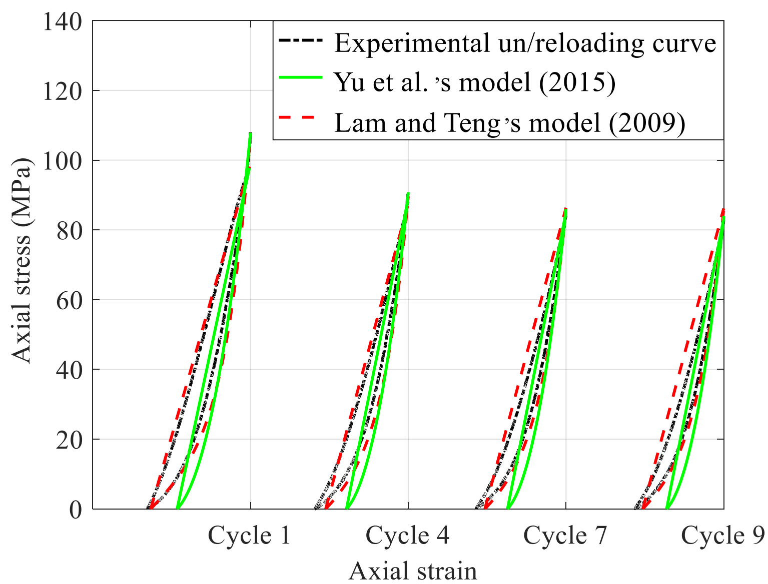

(d) C90-R30-T9-C2

Figure 16. Performance of two models for specimens under loading scheme C2

Table 1. Specimens details

Specimen	GFRP thickness	Mix ratio (%)	Loading scheme
C90-R30-T0-M	0-ply	30	Monotonic
C90-R30-T0-C2	0-ply	30	Cyclic loading scheme 2
C90-R0-T6-M	6-ply	0	Monotonic
C90-R0-T6-C1	6-ply	0	Cyclic loading scheme 1
C90-R0-T6-C2	6-ply	0	Cyclic loading scheme 2
C90-R15-T6-M	6-ply	15	Monotonic
C90-R15-T6-C1	6-ply	15	Cyclic loading scheme 1
C90-R15-T6-C2	6-ply	15	Cyclic loading scheme 2
C90-R30-T6-M	6-ply	30	Monotonic
C90-R30-T6-C1	6-ply	30	Cyclic loading scheme 1
C90-R30-T6-C2	6-ply	30	Cyclic loading scheme 2
C90-R30-T9-M	9-ply	30	Monotonic
C90-R30-T9-C1	9-ply	30	Cyclic loading scheme 1
C90-R30-T9-C2	9-ply	30	Cyclic loading scheme 2

Table 2. Loading schemes for specimens under cyclic axial compression

Specimen	Unloading displacement (mm) found from full-length LVDTs							
	Step 1	Step 2	Step 3	Step 4	Step 5	Step 6	Step 7	Step 8
C90-R30-T0-C2	1.07(4) [a]							
C90-R0-T6-C1	1.02	2.15	3.38	4.14	4.97	5.95		
C90-R0-T6-C2	2.9(8)[a]							
C90-R15-T6-C1	1.00	2.02	3.01	4.00	5.00	6.04		
C90-R15-T6-C2	2.88(9) [a]							
C90-R30-T6-C1	0.94	1.88	2.81	3.77	4.79	5.80	6.76	
C90-R30-T6-C2	2.86(10) [a]							
C90-R30-T9-C1	0.98	2.00	3.02	4.05	5.04	6.04	7.02	8
C90-R30-T9-C2	4.00(9) [a]							

[a] The number in the bracket indicates the number of repeated unloading/reloading cycles imposed at that prescribed unloading displacement value.

Table 3. Key test results of specimens

Specimen	ε_{cu}	f_{cu} (MPa)	ε_{cc}	f_{cc} (MPa)	$\varepsilon_{h,rup}$
C90-R30-T0-M	0.00291	59.0	0.00291	59.0	-
C90-R30-T0-C2	0.00326	60.8	0.00326	60.8	-
C90-R0-T6-M	0.0162	91.0	0.00496	94.4	0.0144
C90-R0-T6-C1	0.0148	91.0	0.00494	94.1	0.0132
C90-R0-T6-C2	0.0162	87.5	0.00503	90.2	0.0146
C90-R15-T6-M	0.0163	76.9	0.0163	76.9	0.0144
C90-R15-T6-C1	0.0161	79.4	0.0161	79.4	0.0142
C90-R15-T6-C2	0.0156	85.6	0.0156	85.6	0.0152
C90-R30-T6-M	0.0154	82.5	0.0154	82.5	0.0154
C90-R30-T6-C1	0.0195	89.6	0.0195	89.6	0.0170
C90-R30-T6-C2	0.0171	85.8	0.0171	85.8	0.0147
C90-R30-T9-M	0.0259	157.1	0.0259	157.1	0.0179
C90-R30-T9-C1	0.0244	142.1	0.0244	142.1	0.0159
C90-R30-T9-C2	0.0291	163.6	0.0291	163.6	.0.0181